

Cite this: DOI: 00.0000/xxxxxxxxxx

Metastable $\text{Cu}_{1-x}\text{CrTe}_2$ – Completing the copper chromium delafossite series through soft chemistryKai D. Röseler,^a Geo Sciarini,^a Felix Eder,^a Samuel Moody,^b Vladimir Pomjakushin,^b and Fabian O. von Rohr^{*a}Received Date
Accepted Date

DOI: 00.0000/xxxxxxxxxx

In the layered copper chromium dichalcogenide series CuCrX_2 , the oxide, the sulfide, and the selenide analogues have been reported, but the telluride CuCrTe_2 has remained unsynthesized so far. Here, we report the synthesis of $\text{Cu}_{1-x}\text{CrTe}_2$ ($x \approx 0.3$), which forms only within a narrow temperature window near 90 °C by solvothermal cation exchange of $\text{K}_{1-x}\text{CrTe}_2$ ($x \approx 0.3$) and CuBr. $\text{Cu}_{1-x}\text{CrTe}_2$ undergoes a magnetostructural transition to an antiferromagnetic state at $T_N = 239$ K, a Néel temperature that is high relative to other ACrTe_2 phases and comparable to that of ferromagnetic, fully-deintercalated CrTe_2 . $\text{Cu}_{1-x}\text{CrTe}_2$ is metastable and decomposes at temperatures as low as 250 °C to form spinel CuCr_2Te_4 . These results highlight the importance of low-temperature topochemical routes for accessing metastable Cu(I)-containing tellurides that are inaccessible by conventional solid-state synthesis.

Introduction

The discovery of new inorganic solids is generally limited because conventional high-temperature synthesis bypasses metastable phases in favor of thermodynamically preferred products.^{1,2} Topochemical reactions, which preserve structural motifs, offer a way around this limitation by operating at low temperatures. They are especially powerful for layered compounds where guest species in the interlayer space can be intercalated,^{3–9} removed,^{10–13} or exchanged.^{14–16} A striking example is 1T- CrTe_2 , a van der Waals ferromagnet with a Curie temperature above room temperature, which is accessible only through topochemical deintercalation of ACrTe_2 ($A = \text{Li}, \text{K}$).^{10,11}

CrX_2 ($X = \text{chalcogen}$) compounds consist of triangular lattices of Cr atoms arranged in layered chalcogenide slabs separated by van der Waals gaps.^{10,17,18} These gaps can accommodate interlayer cations, providing access to the broader ACrX_2 family.^{19–23} In these phases, both the interlayer ion and the chalcogen strongly influence magnetic exchange, transport, and structural distortions, making ACrX_2 compounds a platform for exploring various electronic and magnetic ground states.^{24–26} Beyond the intercalated A cation, the chalcogen itself strongly influences the physical properties, as exemplified in the CuCrX_2 family. Within this family, CuCrO_2 is a transparent p-type semiconductor,²⁷ CuCrS_2 exhibits a remarkably large Seebeck coefficient^{28,29}, and single-layer CuCrSe_2 is a promising multiferroic

candidate.^{30,31} Yet the telluride analogue CuCrTe_2 has not been reported so far. While it has been predicted theoretically to exist as a metallic antiferromagnet.³²

Cr-based tellurides pose a particular synthetic challenge because high-temperature reactions favor competing phases, including NiAs-type Cr_xTe_y compounds such as Cr_2Te_3 .³³ In the Cu–Cr–Te system, an additional thermodynamic sink is provided by the ferromagnetic spinel CuCr_2Te_4 ($T_C = 326$ K),^{34,35} as well as Cu-rich variants $\text{Cu}_{1+y}\text{Cr}_2\text{Te}_4$ ($0 < y \leq 1$) with lower Curie temperatures.³⁶ Already for the lighter chalcogenides, synthesis of the layered phase requires careful temperature control to avoid spinel formation: CuCrS_2 was synthesized at 650 °C to suppress CuCr_2S_4 impurities,²⁸ and CuCrSe_2 is reported to be in equilibrium with CuCr_2Se_4 at temperatures as low as 300 °C.³⁷

In this work, we present the synthesis of $\text{Cu}_{1-x}\text{CrTe}_2$ ($x \approx 0.3$) using a solvent-mediated cation exchange reaction from $\text{K}_{1-x}\text{CrTe}_2$ ($x \approx 0.3$) in comparison to conventional solid-state syntheses and self-flux syntheses, which yielded CuCr_2Te_4 or metal-excessive $\text{Cu}_{1+y}\text{Cr}_2\text{Te}_4$ spinels. We found that $\text{Cu}_{1-x}\text{CrTe}_2$ decomposes as low as 250 °C into the structurally related CuCr_2Te_4 spinel. Using a combined analysis of single-crystal X-ray diffraction, magnetization, and neutron powder diffraction experiments, we identified a magneto-structural transition towards an antiferromagnetic state with $T_N = 239$ K.

^a Department of Quantum Matter Physics, University of Geneva, CH-1211 Geneva, Switzerland.

^b Laboratory for Neutron Scattering and Imaging, Paul Scherrer Institute, CH-5232 Villigen PSI, Switzerland

Experimental

Conventional solid-state syntheses towards CuCrTe₂

Te (pieces, Alfa Aesar, 99.999%) was ground in an agate mortar and mixed with Cu powder (Merck, 99.5%) and Cr powder (Alfa Aesar, 99.95%) in a molar ratio of 2:1:1. The mixture was then pressed into 500 mg pellets with a diameter of 8 mm, placed into quartz tubes (inner diameter 10 mm, thickness 1 mm, length \approx 8.5 cm), and flame sealed under a 300 mbar Ar atmosphere. The sealed silica tubes were placed into box furnaces, which were heated at a rate of 50 K·h⁻¹ to T_x , which was held for 120 h. The maximum temperatures T investigated included 150 °C, 350 °C, and 600 °C.

Self-flux syntheses towards CuCrTe₂

Cu (Merck, 99.5%), Cr (powder, Alfa Aesar, 99.95%) and Te (powder, ground from pieces, Alfa Aesar, 99.999%) in molar ratios of $Z:1:8$ ($Z = 4, 5, 6$) were thoroughly mixed and placed in a Canfield alumina crucible set comprising a bottom and top crucible and a frit separating disc in between³⁸. The set was then sealed in a quartz ampule (inner diameter 12 mm, thickness 1.5 mm, length \approx 11.5 cm) under an Ar atmosphere of 300 mbar. Inside a muffle furnace, the ampule was heated at 30 °C·h⁻¹ to 1000 °C, and was subsequently slow-cooled to 750 °C within 96 h. At 750 °C, the ampule was removed from the oven, and the excess flux was separated by immediate high-temperature centrifugation.

Solvothermal cation exchange reactions towards CuCrTe₂

Solvothermal cation exchange reactions were performed using CuBr as a Cu⁺ source and three different ACrTe₂ phases: (1) Solid-state synthesized K_{1-x}CrTe₂ ($x \approx 0.3$), (2) flux-grown K_{1-x}CrTe₂ ($x \approx 0.3$), and (3) flux-grown LiCrTe₂. Inside an Ar-filled glovebox, 50 mg of the respective ACrTe₂ phases and CuBr (molar ratio 1:10) were placed in Teflon containers with an inner volume of about 16 ml. After the addition of 7 ml dry acetonitrile, the container was closed with a Teflon lid and mounted into a steel autoclave. The autoclave was then heated to 90 °C or 200 °C and it was kept for 7 days under autogenous pressure. Afterward, the oven was turned off, and the autoclave was cooled to room temperature. The autoclave was opened under an Ar atmosphere, and the crystals were transferred into Schlenk tubes. Using standard Schlenk techniques, excess CuBr and KBr were removed by washing the crystals three times with 7 ml of dry acetonitrile, and the crystals were dried under reduced pressure. When increasing the amount of ACrTe₂ to 100 mg, Teflon containers with an inner volume of 44 ml and 14 ml of dry acetonitrile were used instead.

Precursor syntheses

Self-flux syntheses of LiCrTe₂ and K_{1-x}CrTe₂ ($x \approx 0.3$) were conducted as previously reported.^{39,40} For the solid-state synthesis of K_{1-x}CrTe₂ ($x \approx 0.3$), Cr (powder, Alfa Aesar, 99.95%), Te (pieces, Alfa Aesar, 99.999%), and K (block, CALLERY, min 99%) in a molar ratio of 1:1:2 were placed in an alumina crucible. The crucible and an additional crucible on top were flame-sealed in-

side a quartz tube (inner diameter 14 mm, thickness 2 mm, length 8 cm). The quartz tube was then placed inside a box furnace, which was heated at a rate of 30 K·h⁻¹ to 900 °C and held at this temperature for 8 days. The furnace was then cooled at 6 K·h⁻¹ to 450 °C and subsequently at 60 K·h⁻¹ to room temperature.

Powder X-ray diffraction (PXRD)

PXRD data were collected with a Rigaku SmartLabXE diffractometer with Cu-K α radiation ($\lambda = 1.54187$ Å) on a D/teX Ultra 250 detector in capillary mode in the 2θ range of 5–80°. Crystals were ground into fine powders, mixed with starch to minimized effects of preferred orientation, and filled into borosilicate capillaries with an outer diameter of 0.8 mm. Rietveld refinements of the intensity data was performed in the TOPAS-Academic software.⁴¹

Single X-ray diffraction (SXR)

Single X-ray diffraction (SXR) experiments were performed under N₂ cooling at 100 K, 180 K, and 293 K on an Oxford Diffraction Supernova diffractometer using Mo K α radiation ($\lambda = 0.71073$ Å). Pre-experiment screenings, data collection, data reduction, and absorption correction were performed using the program suite CrysAlisPro.⁴² The crystal structure was solved with the dual space method in SHELXT.⁴³ Least squares refinements of F^2 were performed using SHELXL.⁴⁴

Scanning electron microscopy (SEM) and Energy-dispersive X-ray spectroscopy (EDS)

Electron images were obtained from a JEOL JSM-IT800 Scanning electron microscope. Energy dispersive X-ray spectroscopy (EDS) data was collected with an acceleration voltage of 20 kV with an X-Max^N 80 detector from Oxford Instruments. Stoichiometry calculations of Cu_{1-x}CrTe₂ ($x \approx 0.3$) from flux-grown K_{1-x}CrTe₂ ($x \approx 0.3$) crystals are based on 80 point scans on two sites of four crystals from two batches. The same number of measurements was repeated after exfoliation with Scotch tape. Stoichiometry calculations of solid-state synthesized K_{1-x}CrTe₂ ($x \approx 0.3$) and Cu_{1-x}CrTe₂ ($x \approx 0.3$) obtained from it are based on 80 point scans. Before the EDS measurements, solid-state synthesized K_{1-x}CrTe₂ ($x \approx 0.3$) crystals were washed with dry DMF to remove possible potassium-polytelluride side-products on the surface.

Magnetization experiments

Temperature- and field-dependent magnetization measurements were carried out in a Physical Property Measurement System in a cryogen-free system (PPMS DynaCool) from Quantum Design equipped with the vibrating sample magnetometer (VSM) option. $m(T)$ data were recorded in the 1.8–300 K or 1.8–360 K temperature range with a sweep rate of 2 K·min⁻¹, for $m(H)$, an interval of -9 to 9 T was scanned at 50 Oe·s⁻¹.

Neutron powder diffraction

Neutron powder diffraction experiments were performed on the DMC Cold Neutron Diffractometer at the Swiss Spallation Neu-

tron Source from the Paul Scherrer Institute in Villigen, Switzerland. Inside a helium-filled glovebox, finely ground powder of $\text{Cu}_{1-x}\text{CrTe}_2$ ($x \approx 0.3$) obtained from flux-grown $\text{K}_{1-x}\text{CrTe}_2$ ($x \approx 0.3$) was sealed in an aluminum sample container with an inner diameter of 7.5 mm using indium wire. Diffraction data were collected at $T = 2\text{ K}$, $T = 180\text{ K}$, and $T = 240\text{ K}$ with a neutron wavelength of 2.449 \AA . Rietveld refinements were performed using the FullProf Suite package, and the magnetic symmetry was analyzed using ISODISTORT in the ISOTROPY software.^{45,46}

Differential scanning calorimetry (DSC)

Differential scanning calorimetry (DSC) measurement was performed using a Mettler Toledo DSC1 STARe System. Ground $\text{Cu}_{1-x}\text{CrTe}_2$ obtained from solid-state synthesized $\text{K}_{1-x}\text{CrTe}_2$ ($x \approx 0.3$) was placed in an aluminum container, closed with a lid with a small hole for pressure adjustment and heated at a rate of 5 Kmin^{-1} under N_2 atmosphere. The temperature program consisted of two cycles: (1) heating and cooling between RT and $150\text{ }^\circ\text{C}$, and (2) heating and cooling between RT and $300\text{ }^\circ\text{C}$.

Results and Discussion

Synthesis

We explored three synthetic routes towards CuCrTe_2 : conventional solid-state synthesis (CSSS) from the elements, Cu/Te metal-flux reactions, and solvothermal cation exchange. For the latter, three different precursors were used: solid-state synthesized $\text{K}_{1-x}\text{CrTe}_2$ ($x \approx 0.3$), flux-grown $\text{K}_{1-x}\text{CrTe}_2$ ($x \approx 0.3$) crystals, and flux-grown LiCrTe_2 crystals. The reaction conditions tested and products obtained are summarized in Figure 1. Solvothermal cation exchange, of solid-state synthesized and flux-grown $\text{K}_{1-x}\text{CrTe}_2$ ($x \approx 0.3$), at $90\text{ }^\circ\text{C}$ yielded the target phase; all other routes produced CuCr_2Te_4 or Cu-rich spinel variants.

Conventional solid-state synthesis (CSSS): Exemplary conventional solid-state syntheses towards CuCrTe_2 were attempted from the elements at $150\text{ }^\circ\text{C}$, $350\text{ }^\circ\text{C}$, and $600\text{ }^\circ\text{C}$ and the products in the form of black powders were characterized using PXRD and temperature-dependent measurements of the magnetic moment, the results of which are depicted in the SI. After the reaction at $150\text{ }^\circ\text{C}$, the PXRD of the product shows the presence of the unreacted elements and CuTe. At $350\text{ }^\circ\text{C}$, we observed a $\text{Cu}_{1+y}\text{Cr}_2\text{Te}_4$ spinel as well as four reflections, which we could not attribute to any known phase, but did not correspond to the presence of delafossite-type CuCrTe_2 . The PXRD pattern of the sample synthesized at $600\text{ }^\circ\text{C}$ indicates only the presence of the $\text{Cu}_{1+y}\text{Cr}_2\text{Te}_4$ spinel. Measurements of the magnetic moment versus temperature show no magnetic transition between 1.8 K and 360 K for the sample obtained at $150\text{ }^\circ\text{C}$. The sample synthesized at $350\text{ }^\circ\text{C}$ exhibits a ferromagnetic transition at $T_C = 273\text{ K}$ and the sample synthesized at $600\text{ }^\circ\text{C}$ a ferromagnetic transition at $T_C = 163\text{ K}$. Both transition temperatures are well below the reported ferromagnetism below $T_C = 326\text{ K}$ ³⁴ for CuCr_2Te_4 , but within the range of transition temperatures observed for metal-excessive $\text{Cu}_{1+y}\text{Cr}_2\text{Te}_4$ ($0 < y \leq 1$) spinels.³⁶ Furthermore, our results suggest an increase in excess Cu with elevating temperature, which is also in line with an elongation

of the a lattice parameter from $11.2175(4)\text{ \AA}$ ($T_{\text{synth}} = 350\text{ }^\circ\text{C}$) to $11.3203(4)\text{ \AA}$ ($T_{\text{synth}} = 600\text{ }^\circ\text{C}$). No single crystals suitable for SXRD experiments were obtained from these syntheses, but Rietveld refinements using a structural model of a copper-rich $\text{Cu}_{1+y}\text{Cr}_2\text{Te}_4$ could be performed based on the results from self-flux syntheses discussed in the following.

Self-flux synthesis attempts towards CuCrTe_2 : Cu/Te self-flux reactions of molar Cu:Cr:Te ratios of 4:1:8, 5:1:8, and 6:1:8 yielded metallic-black crystals. SXRD on the latter identified the product as a copper-rich spinel with the sum formula of $\text{Cu}_{1.29(3)}\text{Cr}_2\text{Te}_4$. In contrast to the CuCr_2Te_4 spinel, we identified an additional Cu position with low occupancy, leading to partial occupation of otherwise empty tetrahedral voids in the spinel structure. Similar conclusions had been drawn from PXRD measurements of copper-rich $\text{Cu}_{1+y}\text{Cr}_2\text{Te}_4$ spinels earlier.³⁶ The details of our SXRD analysis are given in the SI. EDS measurements on eight crystals of the same batch indicated a sum formula of $\text{Cu}_{1.26(9)}\text{Cr}_{2.08(8)}\text{Te}_4$, which is in good agreement with the sum formula based on the SXRD experiment. Using temperature-dependent measurements of the magnetic moment, we identified a ferromagnetic transition at 284 K , which is slightly lower than the expected T_C of approximately 300 K determined in previous investigations.³⁶ PXRD experiments on crushed crystals confirm the bulk presence of a copper rich spinel. However, it should be noted that CuCr_2Te_4 and copper-rich spinels can hardly be differentiated by PXRD as shown by a comparison of their simulated powder patterns which are presented in the Supplementary Information (SI).

The product of flux-reactions with a lower relative Cu-content (4:1:8) was identified as a mixture of CuCr_2Te_4 or $\text{Cu}_{1+y}\text{Cr}_2\text{Te}_4$, CuTe, as well as a NiAs-type $\text{Cr}_{10.7}\text{Te}_{16}$ phase using PXRD and SXRD experiments. Diffraction and EDS analyses could indicate a doping of $\text{Cr}_{10.7}\text{Te}_8$ with Cu, which is further discussed in the SI. Although metal-flux syntheses have proven to be a useful synthesis strategy for large crystals of the CuCr_2Te_4 spinel, our experiments did not result in the formation of CuCrTe_2 .

Solvothermal cation exchange reactions:

EDS measurements on solid-state synthesized $\text{K}_{1-x}\text{CrTe}_2$ suggest an understoichiometric K-content with an average composition of $\text{K}_{0.74(5)}\text{Cr}_{1.037(22)}\text{Te}_{2.00(5)}$. It should be noted that the composition might be influenced by the holding times or heating rates, which were not specified in detail by Freitas *et al.*¹⁰ Solvothermal cation exchange reactions between solid-state synthesized $\text{K}_{1-x}\text{CrTe}_2$ ($x \approx 0.3$) and CuBr in acetonitrile at $200\text{ }^\circ\text{C}$ yielded the CuCr_2Te_4 spinel. Upon decreasing the synthesis temperature to $90\text{ }^\circ\text{C}$ for one week, careful inspection of the obtained PXRD pattern revealed small but significant differences relative to the simulated pattern of CuCr_2Te_4 and all previous synthesis attempts, especially in the region of $45\text{--}46^\circ 2\theta$. SXRD experiments, discussed in detail in the crystal structure section, identified the obtained crystals as $\text{Cu}_{0.68(3)}\text{CrTe}_2$. These findings suggest that $\text{Cu}_{1-x}\text{CrTe}_2$ can only be synthesized at low temperatures below $200\text{ }^\circ\text{C}$. Cation exchange reactions at $90\text{ }^\circ\text{C}$ were also successful with larger flux-grown $\text{K}_{1-x}\text{CrTe}_2$ crystals, yielding X-ray pure $\text{Cu}_{1-x}\text{CrTe}_2$ crystals with diameters up to 7 mm. Attempts to

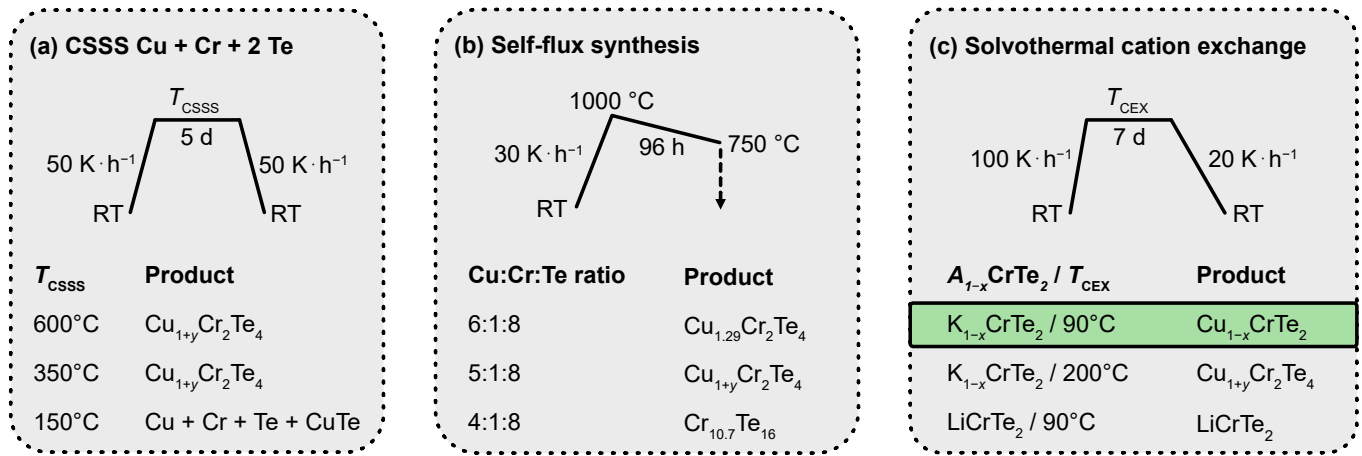


Fig. 1 Overview of attempted syntheses towards CuCrTe_2 and main products obtained. (a) Conventional solid-state synthesis (CSSS), (b) self-flux synthesis, and (c) solvothermal cation exchange reactions. Pictograms depict the temperature program used. In (b), a dashed line represents the centrifugation process. In (c), green color highlights the only successful synthesis of $\text{Cu}_{1-x}\text{CrTe}_2$ ($x \approx 0.3$).

perform cation exchange reactions using LiCrTe_2 at 90°C yielded unreacted LiCrTe_2 and possibly deintercalated CrTe_2 (see additional information in the SI), demonstrating that the successful synthesis of $\text{Cu}_{1-x}\text{CrTe}_2$ is not only temperature-dependent but also precursor-dependent. The larger interlayer distance in $\text{K}_{1-x}\text{CrTe}_2$ compared to LiCrTe_2 appears to favor a topochemical reaction over a significant structural rearrangement.

Crystal structure at room-temperature

The crystal structure of $\text{Cu}_{1-x}\text{CrTe}_2$ was solved from single-crystal X-ray diffraction experiments on $\text{Cu}_{1-x}\text{CrTe}_2$ obtained from solid-state synthesized $\text{K}_{1-x}\text{CrTe}_2$ ($x \approx 0.3$). At 293 K, $\text{Cu}_{0.68(3)}\text{CrTe}_2$ crystallizes in the rhombohedral space group $R\bar{3}m$ with the lattice parameters $a = 3.9180(2) \text{ \AA}$, $c = 20.0120(12) \text{ \AA}$, and $V = 266.04(3) \text{ \AA}^3$. More detailed information on data collection and refinement is listed in Table 2 and the atomic positions are given in Table 1. As depicted in Figure 2, the crystal structure of $\text{Cu}_{0.68(3)}\text{CrTe}_2$ is built from CrTe_2 layers, oriented parallel to (001), which are intercalated by Cu atoms. The CrTe_2 layers consist of edge-sharing CrTe_6 octahedra and follow an ABC-stacking motif. Cu atoms in the interlayer space are coordinated in a distorted tetrahedral geometry, with one Te atom being significantly closer than the other three, which belong to the neighboring layer. The Cu atoms are distributed over partially occupied crystallographic sites with site occupation factors (S.O.F.) of 0.28(2) and 0.40(2), leading to a sum formula of $\text{Cu}_{0.68(3)}\text{CrTe}_2$. Apart from the understoichiometry, $\text{Cu}_{0.68(3)}\text{CrTe}_2$ appears isostructural to other reported MCrX_2 ($M = \text{Cu, Ag, Tl}; X = \text{S, Se}$).^{47,48}

Simulated PXRD patterns based on the structural models of $\text{Cu}_{0.68(3)}\text{CrTe}_2$ and CuCr_2Te_4 (ICSD: 625828) show a degree of similarity (see SI), motivating further investigation of a structural relationship between them.

Figure 2(c) depicts a section of the crystal structure of $\text{Cu}_{0.68(3)}\text{CrTe}_2$. The unit-cell edges of $\text{Cu}_{0.68(3)}\text{CrTe}_2$ are colored black. The grey-colored lines represent a cubic unit cell with $a = 11.24(4) \text{ \AA}$, which is just slightly larger than the reported

CuCr_2Te_4 cell parameter of $a = 11.14 \text{ \AA}$. The cubic unit cell has been drawn between the Cu1 positions.

The basis vectors of the cubic spinel cell ($\mathbf{a}_c, \mathbf{b}_c, \mathbf{c}_c$) are related to those of the delafossite $\text{Cu}_{1-x}\text{CrTe}_2$ cell ($\mathbf{a}, \mathbf{b}, \mathbf{c}$) by:

$$\begin{pmatrix} \mathbf{a} \\ \mathbf{b} \\ \mathbf{c} \end{pmatrix} = \begin{pmatrix} 0 & -\frac{1}{4} & 1 \\ \frac{1}{4} & -\frac{1}{4} & -1 \\ \frac{1}{4} & 0 & 1 \end{pmatrix} \begin{pmatrix} \mathbf{a}_c \\ \mathbf{b}_c \\ \mathbf{c}_c \end{pmatrix} \quad (1)$$

Both crystal structures can be derived from a cubic close packing of Te atoms, and accordingly the Te positions in this idealized cubic cell of $\text{Cu}_{0.68(3)}\text{CrTe}_2$ closely match the cell of CuCr_2Te_4 . The two structures differ, however, in how the octahedral and tetrahedral voids within this packing are occupied. In CuCr_2Te_4 , $\frac{1}{2}$ of the octahedral voids are filled with Cr, forming a 3D network through edge-sharing, and $\frac{1}{8}$ of the tetrahedral voids contain Cu. In $\text{Cu}_{0.68(3)}\text{CrTe}_2$, octahedral coordinated Cr form CrTe_2 layers through edge-sharing, whereas Cu occupies tetrahedral voids in the interlayer space. Additional Cu positions (shown in light green in Figure 2(c)) are present in $\text{Cu}_{0.68(3)}\text{CrTe}_2$ that have no counterpart in the spinel. Because the Cr and Cu sites cannot be fully mapped between the two structures, no group-subgroup relationship can be established.

Crystal structure at 180 K

SXRD measurements at $T = 180 \text{ K}$ on the same single crystal reveal a monoclinic distortion of the unit cell ($a = 6.730(2) \text{ \AA}$, $b = 3.9230(7) \text{ \AA}$, $c = 7.0189(17) \text{ \AA}$, $\beta = 108.31(3)^\circ$, $V = 175.93(8) \text{ \AA}^3$, space group $P2_1/m$ (11)), corresponding to a symmetry reduction from the trigonal $R\bar{3}m$ high-temperature structure. The C-centering expected from a standard trigonal-to-monoclinic descent is absent. This symmetry loss is the result of a disorder-order transition of the Cu atoms in the interlayer space: at $T = 180 \text{ K}$, the Cu1 site refines to a S.O.F. close to 0.5 and was fixed there. A higher occupation factor is unlikely due to close contact between two symmetry-equivalent Cu(I) positions. The Cu2 site has a significantly lower occupancy of 0.135(15). Similar

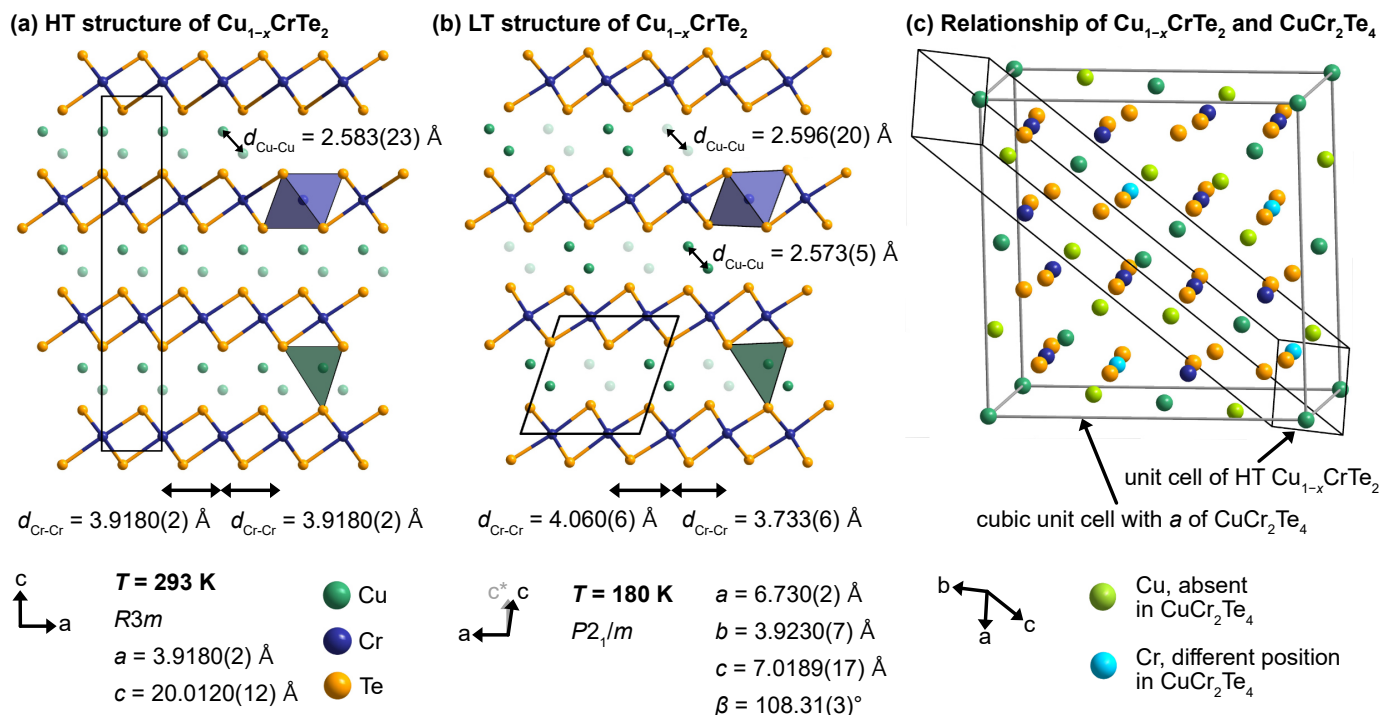


Fig. 2 (a) Crystal structure of HT- $\text{Cu}_{0.68(3)}\text{CrTe}_2$ at $T = 293 \text{ K}$ viewed along the b axis. Cu atoms are colored green, Cr blue, and Te orange. Polyhedra show the octahedral coordination of Cr (blue) and the tetrahedral coordination of Cu (green). (b) Monoclinic distorted crystal structure of LT- $\text{Cu}_{0.635(16)}\text{CrTe}_2$ at $T = 180 \text{ K}$ viewed along the b axis. Transparency of the Cu atoms is set to $1 - 2 \cdot (\text{S.O.F.})$. (c) Similarities of the crystal structures of HT- $\text{Cu}_{0.68(3)}\text{CrTe}_2$ and CuCr_2Te_4 . Dark lines show the unit cell of HT- $\text{Cu}_{0.68(3)}\text{CrTe}_2$ and grey lines a cubic unit cell with $a = 11.24(4) \text{ \AA}$ similar to the unit cell of CuCr_2Te_4 . Cu atom positions present in HT- $\text{Cu}_{0.68(3)}\text{CrTe}_2$ but not CuCr_2Te_4 are colored light-green. Cr atom positions that differ between the two crystal structures are colored light-blue. Cu2 atoms in (c) are omitted for clarity.

order-disorder transitions have been reported for CuCrSe_2 at $T = 365 \text{ K}$ and for CuCrS_2 at $T = 688 \text{ K}$.^{31,49} The transition to the low-temperature modification coincided with a (threefold) twinning by the former threefold rotation axis.

The structural transition also breaks the symmetry of the Cr sublattice. At $T = 293 \text{ K}$, the Cr atoms are equidistantly spaced in a triangular lattice ($d_{\text{Cr-Cr}} = 3.9180(2) \text{ \AA}$), whereas at $T = 180 \text{ K}$ three distinct Cr-Cr distances emerge: $d_{\text{Cr-Cr}} = 3.733(6) \text{ \AA}$, $d_{\text{Cr-Cr}} = 3.9230(7) \text{ \AA}$ and $d_{\text{Cr-Cr}} = 4.060(6) \text{ \AA}$. As discussed in the magnetic properties section (see below), this distortion is directly linked to the antiferromagnetic spin arrangement. The Cu-Cu distances remain comparable between 293 K and 180 K, ranging from 2.573(5) to 2.596(20) \AA , which is slightly longer than the Cu-Cu distance of 2.304(16) \AA reported for disordered CuCrSe_2 .⁴⁹

Microstructure and elemental composition

SEM images at various magnifications of $\text{Cu}_{1-x}\text{CrTe}_2$ ($x \approx 0.3$) synthesized both from flux-grown and solid-state synthesized $\text{K}_{1-x}\text{CrTe}_2$ ($x \approx 0.3$) (see SI) show plate-like crystals with terraced surface features, consistent with the layered character of the crystal structure. The Br content is negligible, with 0.4(5) mol% and 0.9(12) mol% respectively, indicating that the washing procedure effectively removed KBr from the product. The remaining elemental compositions of $\text{Cu}_{0.70(3)}\text{K}_{0.050(20)}\text{Cr}_{0.99(4)}\text{Te}_{2.00(3)}$ and $\text{Cu}_{0.75(3)}\text{K}_{0.025(15)}\text{Cr}_{1.018(23)}\text{Te}_{2.00(3)}$, respectively, are in good agreement with SXRD. Both samples contain trace amounts of

Table 1 Crystallographic sites in $\text{Cu}_{1-x}\text{CrTe}_2$ ($x \approx 0.3$) including site occupation factors (S.O.F.) and Wyckoff positions at 293 K in $R3m$ (160) and at 180 K in $(P2_1/m)$ (11). The respective structural parameters are listed in Table 2. Data for $T = 100 \text{ K}$ is listed in the SI.

$T = 293 \text{ K}$					
Site	Wyckoff	S.O.F.	x	y	z
Cu1	3a	0.28(2)	2/3	1/3	0.505(2)
Cu2	3a	0.40(2)	1/3	2/3	0.5673(12)
Cr1	3a	1	2/3	1/3	0.3741(8)
Te1	3a	1	1/3	2/3	0.44805(7)
Te2	3a	1	2/3	1/3	0.62763(15)
$T = 180 \text{ K}$					
Site	Wyckoff	S.O.F.	x	y	z
Cu1	2e	0.5	0.8870(9)	1/4	0.4068(7)
Cu2	2e	0.135(15)	0.617(4)	1/4	0.593(3)
Cr1	2e	1	0.7348(6)	1/4	0.9965(5)
Te1	2e	1	1.0075(2)	1/4	0.7790(2)
Te2	2e	1	0.4915(2)	1/4	0.2432(2)

K from the precursor, corresponding to an exchange of over 93% and 96% of the initial K content. Although the K concentration is close to the EDS detection limit and the K and Te lines overlap spectrally, elemental mapping (see SI) confirms a homogeneous distribution of all elements with no evidence of unreacted $\text{K}_{1-x}\text{CrTe}_2$.

Thermal stability

To investigate the thermal stability and decomposition of $\text{Cu}_{1-x}\text{CrTe}_2$ ($x \approx 0.3$) under inert atmosphere, we performed DSC

Table 2 Single-crystal X-ray diffraction data for $\text{Cu}_{1-x}\text{CrTe}_2$ at 293 K (trigonal high-temperature phase), 180 K, and 100 K (monoclinic low-temperature phase). Crystals were obtained by solvothermal cation exchange of solid-state synthesized $\text{K}_{1-x}\text{CrTe}_2$ ($x \approx 0.3$). Information on the crystallographic sites is listed in Table 1. Data at the three different temperatures was collected on the same single crystal.

Physical, crystallographic, and analytical data			
	HT-$\text{Cu}_{0.68(3)}\text{CrTe}_2$	LT-$\text{Cu}_{0.635(16)}\text{CrTe}_2$	LT-$\text{Cu}_{0.637(19)}\text{CrTe}_2$
Chemical formula	$\text{Cu}_{0.68(3)}\text{CrTe}_2$	$\text{Cu}_{0.635(16)}\text{CrTe}_2$	$\text{Cu}_{0.637(19)}\text{CrTe}_2$
CCDC Deposition code	2554011	2554012	2554014
Mol. wt. ($\text{g}\cdot\text{mol}^{-1}$)	350.38	347.55	347.55
Cryst. syst.	trigonal	monoclinic	monoclinic
Space group	$R\bar{3}m$ (160)	$P2_1/m$ (11)	$P2_1/m$ (11)
a (Å)	3.9180(2)	6.730(2)	6.6599(8)
b (Å)	–	3.9230(7)	3.9186(4)
c (Å)	20.0120(12)	7.0189(17)	6.9993(8)
β (°)	–	108.31(3)	108.275(12)
V (Å ³)	266.04(3)	175.93(8)	173.45(4)
Z	3	2	2
Calculated density ($\text{g}\cdot\text{cm}^{-3}$)	6.561	6.561	6.655
Temperature (K)	292.99(12)	180.00(10)	99.9(2)
Diffractometer	Rigaku XtaLAB Synergy-S	Rigaku Oxford Diffraction SuperNova	Rigaku XtaLAB Synergy-S
Radiation (λ)	Mo $K\alpha$ (0.71073 Å)	Mo $K\alpha$ (0.71073 Å)	Mo $K\alpha$ (0.71073 Å)
Crystal color	black	black	black
Crystal description	plate	plate	plate
Crystal size (mm^3)	$0.13 \times 0.11 \times 0.02$	$0.13 \times 0.13 \times 0.03$	$0.13 \times 0.13 \times 0.03$
Linear absorption coefficient (mm^{-1})	23.026	22.952	23.280
Scan mode	ω	ω	ω
Recording range θ (°)	3.054 to 30.539	3.057 to 30.578	2.9610 to 30.7790
h range	$-5 \leq h \leq +5$	$-9 \leq h \leq +9$	$-9 \leq h \leq +9$
k range	$-5 \leq k \leq +5$	$-5 \leq k \leq +5$	$-5 \leq k \leq +5$
l range	$-28 \leq l \leq +28$	$-10 \leq l \leq +10$	$-10 \leq l \leq +10$
Nr. of measured reflections	2456	3140	5441
Data reduction			
Completeness (%)	100	100	100
Nr. of independent reflections	262	612	602
R_{int} (%)	3.45	5.19	5.16
R_{σ} (%)	1.08	3.26	1.85
Absorption correction	numerical (Gaussian grid)	numerical (Gaussian grid)	numerical (Gaussian grid)
Independent reflections with $I \geq 2.0\sigma$	262	505	562
Refinement			
$R1$ (obs / all) (%)	4.45/4.45	7.21/8.43	8.36/8.61
$wR2$ (obs / all) (%)	11.91/11.91	18.23/19.13	22.50/22.74
GOF	1.249	1.194	1.144
Nr. of refined parameters	17	32	32
Nr. of restraints	1	0	0
Difference Fourier residues ($e^{-\text{Å}^{-3}}$)	-2.95, 3.99	-4.84, 5.11	-6.42, 4.61

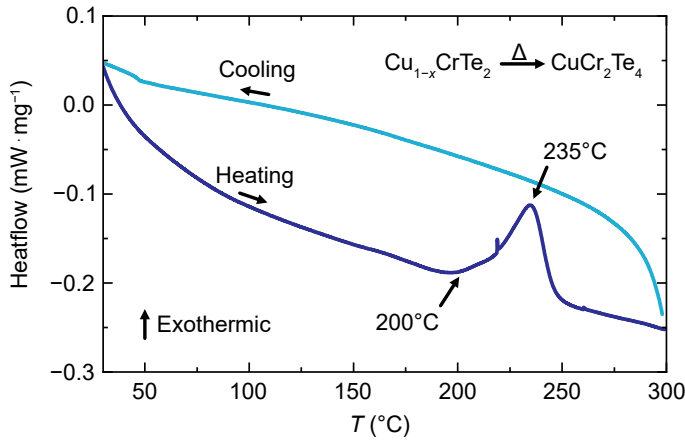


Fig. 3 DSC measurement on $\text{Cu}_{1-x}\text{CrTe}_2$ ($x \approx 0.3$) between RT and 300 °C. The dark-blue line represents the DSC heat flow signal upon heating and the light-blue line upon cooling. An increasing DSC signal corresponds to an exothermic event, associated with the decomposition of $\text{Cu}_{1-x}\text{CrTe}_2$. Arrows point to the onset and maximum of the decomposition signal.

measurements on ground $\text{Cu}_{1-x}\text{CrTe}_2$ ($x \approx 0.3$) crystals obtained from a solvothermal cation exchange reaction from solid-state synthesized $\text{K}_{1-x}\text{CrTe}_2$ ($x \approx 0.3$). The temperature program consisted of two cycles: (1) heating and cooling between RT and 150 °C, and (2) heating and cooling between RT and 300 °C.

During the first heating (and cooling) between RT and 150 °C (see SI), no exothermic or endothermic signal was observed, suggesting thermal stability around the employed synthesis temperature of 90 °C. Upon the second heating, an exothermic event with an onset at $T \approx 200$ °C and a maximum at $T \approx 235$ °C is observed. Upon cooling to RT no thermal signal was detected, suggesting that the exothermic event at $T \approx 200$ °C corresponds to an irreversible decomposition. To confirm this, powdered $\text{Cu}_{1-x}\text{CrTe}_2$ ($x \approx 0.3$) was tempered at 250 °C for 48 h in a quartz ampule. PXRD experiments on the tempered powder identified it as CuCr_2Te_4 (see SI), confirming the thermal decomposition of $\text{Cu}_{1-x}\text{CrTe}_2$ ($x \approx 0.3$) to CuCr_2Te_4 at approximately 200 °C. This finding is also in line with our solvothermal cation-exchange reactions at 200 °C which directly yielded the CuCr_2Te_4 spinel. Temperature-dependent measurements of the magnetic moment of CuCr_2Te_4 obtained by tempering $\text{Cu}_{1-x}\text{CrTe}_2$ ($x \approx 0.3$) are depicted in the SI. The sample exhibits a single ferromagnetic transition at $T_C = 327$ K as previously reported for CuCr_2Te_4 .³⁴

Magnetic properties

To determine the magnetic structure of $\text{Cu}_{1-x}\text{CrTe}_2$ ($x \approx 0.3$), neutron powder diffraction (NPD) data were collected, and magnetization measurements were performed. For the NPD, crushed crystals synthesized from flux-grown $\text{K}_{1-x}\text{CrTe}_2$ ($x \approx 0.3$) were measured at $T = 240$ K, 180 K, and 2 K. The refined NPD data are shown in 4(a). The 240 K pattern is well described by the trigonal-rhombohedral high-temperature nuclear structure. At 180 K, additional reflections appear that cannot be attributed to the monoclinic low-temperature nuclear structure. Using the

search program in the FullProf suite, these were identified as magnetic reflections described by the propagation vector $k = (0.5, 0, 0.5)$. Of the four one-dimensional irreducible representations compatible with this k -vector and the $P2_1/m$ space group (determined using ISODISTORT; see SI for details), the best fit is obtained with the magnetic space group P_a2_1/m with origin at (0,0,0) (BNS No. 11.55, UNI $P2_1/m.1'_a[P2_1/m]$). From the parent space group $P2_1/m$ to the MSG P_a2_1/m a $\{(2,0,0), (0,-1,0), (-1,0,-1)\}$ basis transformation was made. The resulting magnetic structure based on the Rietveld refinement at 180 K is shown in Figure 4(b). At 180 K, the refined spin arrangement is overall antiferromagnetic. Cr atoms separated by the shorter distance ($d_{\text{Cr-Cr}} = 3.733(6)$ Å) couple antiferromagnetically, while those at the larger distance ($d_{\text{Cr-Cr}} = 4.060(6)$ Å) couple ferromagnetically. This is consistent with the Goodenough–Kanamori–Anderson rules:^{50–54} the shorter Cr–Cr pairs correspond to sharper Cr–Te–Cr angles, favoring antiferromagnetic direct exchange, whereas Cr–Te–Cr angles closer to 90° favor ferromagnetic superexchange. NPD data collected at $T = 2$ K do not show significant differences compared to those at 180 K, suggesting no further structural transitions, but resulted in slightly worse refinement parameters.

Temperature-dependent magnetization measurements (Figure 4(c); full data set in the SI) support the antiferromagnetic ordering. At applied fields of 1 T and 5 T, a clear transition is observed at $T_N = 239$ K. An additional ferromagnetic-like feature appears near 115–122 K. This transition closely matches the Curie temperature of the $\text{K}_{1-x}\text{CrTe}_2$ precursor ($T_C = 116$ K) and we attribute it to trace amounts of unreacted precursor, whose ferromagnetic signal can dominate even at low concentrations due to its higher net moment, as no change in the long-range magnetic order in the NPD data is observed.

Table 3 Comparison of refined parameters of neutron powder diffraction data on $\text{Cu}_{1-x}\text{CrTe}_2$ synthesized from flux-grown $\text{K}_{1-x}\text{CrTe}_2$ ($x \approx 0.3$) collected at $T = 240$ K, 180 K and 2 K. ccc

Temperature (K)	240	180	2
Space group	$R\bar{3}m$	P_a2_1/m	P_a2_1/m
a (Å)	3.9399(4)	13.4137(23)	13.3712(26)
b (Å)	–	3.9503(10)	3.9446(11)
c (Å)	20.030(5)	8.0436(22)	8.0291(23)
β (°)	–	124.201(24)	124.228(22)
Origin	–	(0/0/0)	(0/0/0)
m_b (μ_B)	–	1.56(6)	1.89(6)
R_p	6.25	6.32	6.57
R_{wp}	8.03	8.11	8.42
R_{exp}	2.76	2.30	1.81
χ^2	8.43	12.5	21.5

Conclusions

We have synthesized $\text{Cu}_{1-x}\text{CrTe}_2$ ($x \approx 0.3$), the previously missing telluride member of the CuCrX_2 series. We find this phase to exist only within a narrow thermodynamic window. The compound is bound by unreacted precursors at low temperatures and decomposes into the structurally related CuCr_2Te_4 spinel at temperatures as low as 200 °C. This narrow stability window renders conventional high-temperature routes ineffective and explains why

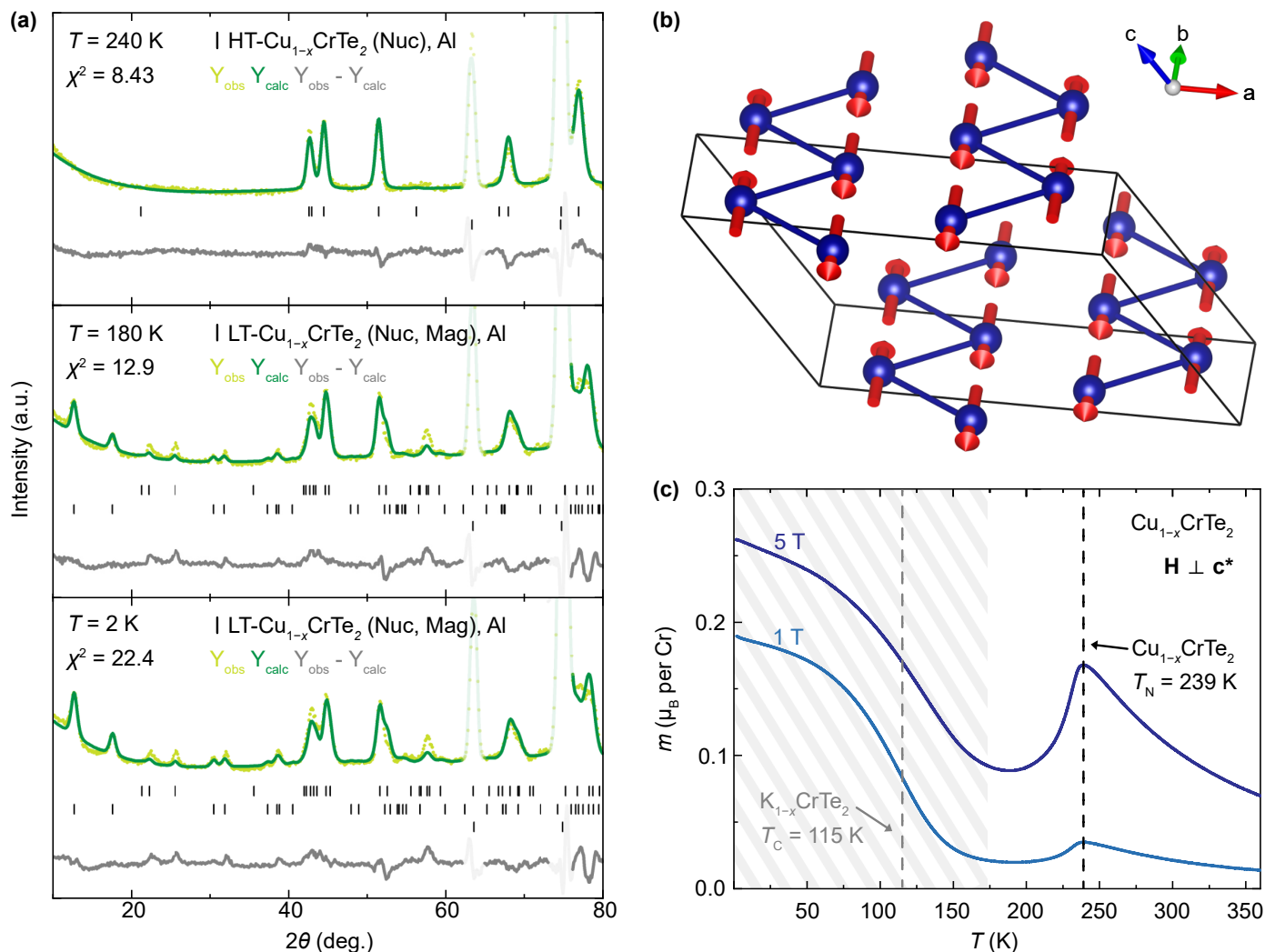


Fig. 4 (a) Refined neutron powder diffraction patterns of $\text{Cu}_{1-x}\text{CrTe}_2$ ($x \approx 0.3$) collected with a neutron wavelength of 2.449 \AA at $T = 240$ K, 180 K, and 2 K. Observed intensities are colored light-green, calculated intensities dark-green, differences in grey, and Bragg positions in black. 2θ intervals of $62\text{--}65^\circ$ and $73\text{--}76^\circ$ are partially transparent for clarity due to strong intensities from the Al container. Full patterns are depicted in the SI. The order of observed phases (left to right) corresponds to the line order of Bragg positions (top to bottom). "Nuc" represents a nuclear only, structural contribution, and "Mag" a purely magnetic contribution. (b) Magnetic structure of $\text{Cu}_{1-x}\text{CrTe}_2$ ($x \approx 0.3$). For clarity, only Cr atoms are depicted with red arrows indicating the direction of the magnetic moments. Cr–Cr bonds are depicted to differentiate between closer and more distant Cr atoms. (c) Temperature-dependent measurements of the magnetic moment of $\text{Cu}_{1-x}\text{CrTe}_2$ ($x \approx 0.3$) between 1.8 K and 360 K for magnetic fields of 1 T and 5 T applied perpendicular to \mathbf{c}^* .

CuCrTe_2 has remained unreported until now. Nearly phase-pure samples were obtained here by solvothermal cation exchange at 90°C , preserving the layered topology of the $\text{K}_{1-x}\text{CrTe}_2$ precursor.

We found that $\text{Cu}_{1-x}\text{CrTe}_2$ ($x \approx 0.3$) exhibits robust magnetic order. Neutron powder diffraction reveals an antiferromagnetic ground state below $T_N = 239$ K, accompanied by a structural transition from a trigonal-rhombohedral to a monoclinic unit cell. The Néel temperature is notably high within the $M\text{CrTe}_2$ family and comparable to the ferromagnetic ordering temperature of fully deintercalated CrTe_2 . The antiferromagnetic spin arrangement obeys the Goodenough–Kanamori–Anderson rules, with the coupling sign governed by the Cr–Te–Cr bond angle. The successful use of solvothermal cation exchange at mild temperatures suggests that similar strategies may provide a route to other missing members of the $M\text{CrX}_2$ family and related intercalated van der

Waals compounds.

Author contributions

FvR designed the experiments. KR and GS synthesized the crystals. KR, GS, FE, VP, and SM conducted the measurements. All authors contributed to the analysis of the data. FvR and KR wrote the manuscript with contributions from all the authors.

Conflicts of interest

There are no conflicts to declare.

Data availability

Crystallographic data for the LT and HT structures of $\text{Cu}_{1-x}\text{CrTe}_2$ and $\text{Cu}_{1.29}\text{Cr}_2\text{Te}_4$ have been deposited at the Cambridge Crystallographic Data Centre under deposition numbers CCDC 2554011-

2554014. These data can be obtained free of charge from the CCDC via www.ccdc.cam.ac.uk/data_request/cif. Mcif files of the neutron refinements will be provided in the MAGNDATA database. All other data supporting the findings of this study are available within the article and its Supplementary Information.

Acknowledgements

This work was supported by the Swiss National Science Foundation under grants No. PCEFP2_194183 and No. 200021-204065. Part of this work was performed at the Swiss Spallation Neutron Source (SINQ), Paul Scherrer Institut (PSI), Villigen, Switzerland. The authors would like to thank the UNIGE crystallography service for their help with establishing the structural relationship and Kerry Lee Paglia for conducting the DSC measurement.

Notes and references

- 1 M. Jansen, *Angewandte Chemie International Edition*, 2002, **41**, 3746–3766.
- 2 D. L. M. Cordova and D. C. Johnson, *ChemPhysChem*, 2020, **21**, 1345–1368.
- 3 S. F. Meyer, R. E. Howard, G. R. Stewart, J. V. Acrivos and T. H. Geballe, *The Journal of Chemical Physics*, 1975, **62**, 4411–4419.
- 4 N. D. Kelly, H. Grievson, K. M. Steele, I. da Silva and S. J. Clarke, *Dalton Trans.*, 2025, **54**, 8123–8132.
- 5 T. Hatakeda, T. Noji, T. Kawamata, M. Kato and Y. Koike, *Journal of the Physical Society of Japan*, 2013, **82**, 123705.
- 6 P. A. Hyde, M. Avdeev, N. H. Rees and S. J. Clarke, *Chemistry of Materials*, 2024, **36**, 9939–9946.
- 7 P. A. Hyde, J. Cen, S. J. Cassidy, N. H. Rees, P. Holdship, R. I. Smith, B. Zhu, D. O. Scanlon and S. J. Clarke, *Inorganic Chemistry*, 2023, **62**, 12027–12037.
- 8 P. Witte, A. M. van Koten and M. E. Kamminga, *Materials Advances*, 2024, **5**, 6702–6718.
- 9 D. Tezze, C. Álvarez-García, D. Margineda, M. Furqan, S. Mattioni, J. M. Pereira, U. Ahsan, V. Mazanek, Y. K. Maurya, I. Abdel Aziz *et al.*, *Nature Synthesis*, 2026, **5**, 388–397.
- 10 D. C. Freitas, R. Weht, A. Sulpice, G. Remenyi, P. Strobel, F. Gay, J. Marcus and M. Núñez-Regueiro, *Journal of Physics: Condensed Matter*, 2015, **27**, 176002.
- 11 K. D. Röseler, C. Witteveen, C. Besnard, V. Pomjakushin, H. O. Jeschke and F. O. von Rohr, *Journal of Materials Chemistry A*, 2025.
- 12 X. Zhou, B. Wilfong, H. Vivanco, J. Paglione, C. M. Brown and E. E. Rodriguez, *Journal of the American Chemical Society*, 2016, **138**, 16432–16442.
- 13 A. Mantravadi, B. C. Weaver, S. Chen, S. Mukta, Y. Abusa, A. Sarkar, Y. Sun, Y. Mudryk, A. Gundlach-Graham, K.-M. Ho *et al.*, *Journal of the American Chemical Society*, 2024, **146**, 26786–26800.
- 14 S. Aharon, S. Chatterjee, F. Yuan, G. Carrel, J. Xie, T. Berry, B. L. Hoff and L. M. Schoop, *Zeitschrift für anorganische und allgemeine Chemie*, 2025, **651**, e202500098.
- 15 A. Sethi, D. K. Yadav and S. Uma, *Ceramics International*, 2022, **48**, 13833–13841.
- 16 X. Song, Z. Liu, E. F. Seewald, A. K. Kundu, D. Muñoz-Segovia, M.-G. Han, S. R. Docherty, D. G. Chica, J. P. Ingham, J. Li *et al.*, *Journal of the American Chemical Society*, 2025, **147**, 37833–37841.
- 17 X. Song, G. Cheng, D. Weber, F. Pielhofer, S. Lei, S. Klemenz, Y.-W. Yeh, K. A. Filsinger, C. B. Arnold, N. Yao *et al.*, *Journal of the American Chemical Society*, 2019, **141**, 15634–15640.
- 18 C. Van Bruggen, R. Haange, G. Wiegers and D. De Boer, *Physica B+ C*, 1980, **99**, 166–172.
- 19 F. Engelsman, G. Wiegers, F. Jellinek and B. Van Laar, *Journal of Solid State Chemistry*, 1973, **6**, 574–582.
- 20 K. D. Röseler, F. Eder and F. O. von Rohr, *Chemistry—A European Journal*, 2026, e70897.
- 21 X. Song, S. N. Schneider, G. Cheng, J. F. Khoury, M. Jovanovic, N. Yao and L. M. Schoop, *Chemistry of Materials*, 2021, **33**, 8070–8078.
- 22 F. Eder, C. Witteveen, E. Giannini and F. O. von Rohr, *Journal of the American Chemical Society*, 2025, **147**, 4896–4903.
- 23 F. Eder, C. Witteveen, E. Giannini and F. O. von Rohr, *Chemistry of Materials*, 2025, **37**, 9204–9211.
- 24 S. Kobayashi, H. Ueda, C. Michioka and K. Yoshimura, *Inorganic Chemistry*, 2016, **55**, 7407–7413.
- 25 E. Nocerino, S. Kobayashi, C. Witteveen, O. K. Forslund, N. Matsubara, C. Tang, T. Matsukawa, A. Hoshikawa, A. Koda, K. Yoshimura *et al.*, *Communications Materials*, 2023, **4**, 81.
- 26 E. Nocerino, C. Witteveen, S. Kobayashi, O. K. Forslund, N. Matsubara, A. Zubayer, F. Mazza, S. Kawaguchi, A. Hoshikawa, I. Umegaki *et al.*, *Scientific Reports*, 2022, **12**, 21657.
- 27 L. Farrell, E. Norton, C. M. Smith, D. Caffrey, I. V. Shvets and K. Fleischer, *J. Mater. Chem. C*, 2016, **4**, 126–134.
- 28 G. C. Tewari, T. S. Tripathi and A. K. Rastogi, *Journal of Electronic Materials*, 2010, **39**, 1133–1139.
- 29 A. Romanenko, G. Chebanova, T. Chen, W. Su and H. Wang, *Journal of Physics D: Applied Physics*, 2022, **55**, 143001.
- 30 Z. Sun, Y. Su, A. Zhi, Z. Gao, X. Han, K. Wu, L. Bao, Y. Huang, Y. Shi, X. Bai, P. Cheng, L. Chen, K. Wu, X. Tian, C. Wu and B. Feng, *Nature Communications*, 2024, **15**, 4252.
- 31 M. T. Rahman, N. P. Holzapfel, K. Ciesielski, W. Guetari, E. Toberer, V. Augustyn and A. Zevalkink, *Chemistry of Materials*, 2025, **37**, 6718–6726.
- 32 D. Srivastava, G. C. Tewari, M. Karppinen and R. M. Nieminen, *Journal of Physics: Condensed Matter*, 2013, **25**, 105504.
- 33 G. Chattopadhyay, *Journal of Phase Equilibria*, 1994, **15**, 431–440.
- 34 T. Suzuyama, J. Awaka, H. Yamamoto, S. Ebisu, M. Ito, T. Suzuki, T. Nakama, K. Yagasaki and S. Nagata, *Journal of Solid State Chemistry*, 2006, **179**, 140–144.
- 35 T. Koneshova and N. Kudryashov, *Russian Journal of Inorganic Chemistry*, 2014, **59**, 609–613.
- 36 F. Lotgering and G. van der Steen, *Solid State Communications*, 1971, **9**, 1741–1744.
- 37 E. G. Shkvarina, A. S. Shkvarin, A. A. Titov, M. S. Postnikov, J. R. Plaisier, L. Gigli, M. Gaboardi and A. N. Titov, *Journal of*

- Solid State Chemistry*, 2024, **330**, 124497.
- 38 P. C. Canfield, T. Kong, U. S. Kaluarachchi and N. H. Jo, *Philos. Mag.*, 2016, **96**, 84–92.
- 39 C. Witteveen, E. Nocerino, S. A. López-Paz, H. O. Jeschke, V. Y. Pomjakushin, M. Månsson and F. O. von Rohr, *Journal of Physics: Materials*, 2023, **6**, 035001.
- 40 C. Witteveen, *PhD thesis*, 2025.
- 41 A. Coelho, *Journal of Applied Crystallography*, 2018, **51**, 210–218.
- 42 O. D. Rigaku, *Rigaku Oxford Diffraction Ltd, Yarnton, Oxfordshire, England*, 2015.
- 43 G. Sheldrick, *Acta Crystallographica Section A*, 2015, **71**, 3–8.
- 44 G. M. Sheldrick, *Acta Crystallographica Section C*, 2015, **71**, 3–8.
- 45 H. T. Stokes, D. M. Hatch and B. J. Campbell, *ISODISTORT, ISOTROPY Software Suite*, iso.byu.edu.
- 46 H. T. Stokes, D. M. Hatch and B. J. Campbell, *Journal of Applied Crystallography*, 2006, **39**, 607.
- 47 H. Hahn and C. D. Lorent, *Zeitschrift für anorganische und allgemeine Chemie*, 1957, **290**, 68–81.
- 48 M. Rosenberg, A. Knülle, H. Sabrowsky and C. Platte, *Journal of Physics and Chemistry of Solids*, 1982, **43**, 87–95.
- 49 A. Gagor, D. Gnida and A. Pietraszko, *Materials Chemistry and Physics*, 2014, **146**, 283–288.
- 50 P. W. Anderson, *Phys. Rev.*, 1950, **79**, 350–356.
- 51 J. B. Goodenough, *Phys. Rev.*, 1955, **100**, 564–573.
- 52 J. B. Goodenough, *Journal of Physics and Chemistry of Solids*, 1958, **6**, 287–297.
- 53 J. Kanamori, *Progress of Theoretical Physics*, 1957, **17**, 177–196.
- 54 J. Kanamori, *Progress of Theoretical Physics*, 1957, **17**, 197–222.